Optimized Design of AC-Side Inductance for Grid-Forming Inverters

Lei GAO, Jing LYU, Jinshui DAI, Han WANG, and Xu CAI

***Abstract*—With the large-scale integration of renewable energy into modern power systems, grid-forming (GFM)-based inverters will play an increasingly important role. Currently, the design approach for the AC-side inductance of filter in GFM inverters still follows that of grid-following (GFL)-based inverters, potentially hindering optimal performance. To tackle this issue, an optimized design method for the AC-side inductance of GFM inverters is proposed in this paper by taking into account the specific requirements of various applications. Furthermore, a customized parameter design method for the AC-side inductance is introduced, aiming to achieve a balance between dynamic performance needs and control challenges. Finally, the validation of the proposed optimized design method is demonstrated through simulations and experimental results obtained from the Modeling Tech StarSim controller hardware-in-the-loop platform.**

***Index Terms*—AC-side inductance, grid-forming inverters, grid-following inverters, inertia synchronization control, optimized design, virtual synchronous generator control.**

I. INTRODUCTION

IN recent years, the safe and stable operation of the power system has encountered significant challenges due to the proliferating integration of grid-following (GFL) inverter-based renewable energy generation units [1]. Unlike synchronous machines, GFL inverter-based resources lack an inherent "swing equation" that naturally synchronizes them with the grid [2]. The integration of an increasing number of GFL inverter-based resources into the power system has contributed to a reduction in system inertia and a decline in the short-circuit ratio (SCR), thereby undermining the synchronous stability of modern power systems [3]. Conversely, grid-forming (GFM) inverter technology has demonstrated robust performance in standalone mode as well as in weak grids [4]. Operating as controllable voltage sources, GFM inverters effectively address the synchronous stability challenges faced by traditional GFL inverter-based resources.

The concept of GFM inverters, originally introduced for microgrid and islanded grid applications, has been proposed as a feasible solution for enhancing the stability and resilience of larger interconnected power networks with a high penetration of power electronics-based generation [5]. The GFM control technology, which possesses the capability to augment system inertia and damping, is emerging as a highly promising approach for future power grids. Currently, GFM controls primarily include virtual synchronous generator (VSG) control [6], [7], power synchronization control (PSC) [8], inertia synchronization control (ISynC) [9], and so on.

To enhance the dynamic performance of GFM inverters, numerous studies have focused on optimizing control parameters for various GFM control methods [6]–[10]. However, limited attention has been paid to the design of AC-side inductance for GFM inverters. The AC-side inductor, as a fundamental component in the main circuit of grid-connected inverters, plays a crucial role in determining the system's dynamic performance and harmonic suppression capabilities [11], [12]. Lower inductance values can improve transient response but might compromise harmonic suppression. Conversely, higher inductance values can effectively suppress current ripples and present superior filtering performance, but they may reduce the power factor, and increase voltage drop across the inductor, thereby affecting the power transmission capacity of the grid-connected inverter [13].

The conventional approach for AC-side inductance parameter design initially involves calculations based on constraints, including current harmonics [14]–[16] and four-quadrant operation [16]–[19]. However, the design methodology for the AC-side inductance of GFM inverters often follows that of GFL inverters, potentially hindering the achievement of optimal performance for GFM inverters. The optimization of AC-side inductance requires balancing multiple competing objectives including minimizing harmonic distortion [20] maintaining four-quadrant power-flow characteristics [16]–[19] mitigating power coupling [21], and enhancing anti-disturbance capabilities [22], limiting the fault current [23], etc. The inductance value is supposed to strike a balance between these competing objectives.

The complexity of inductance parameter optimization for GFM inverters is further compounded by the specific requirements of different applications. For instance, the output active and reactive powers of the GFM inverters are regulated through the active and reactive power controls, such as droop control

---

Manuscript received July 8, 2025; revised September 1, 2025; accepted December 22, 2025. Date of publication March 30, 2026; date of current version February 2, 2026. This work was supported by the National Natural Science Foundation of China under Grant 52277195. (*Corresponding author: Jing Lyu.*)

All authors are with the Key Laboratory of Control of Power Transmission and Conversion, Ministry of Education, School of Electrical Engineering, Shanghai Jiao Tong University, Shanghai 200240, China (e-mail: gaolei97@sjtu.edu.cn; lvjing@sjtu.edu.cn; jshdai@sjtu.edu.cn; wanghansjtu@sjtu.edu.cn; xucai@sjtu.edu.cn).

Digital Object Identifier 10.24295/CPSSTPEA.2025.00042

[24], PSC [25], and virtual synchronous generator [6], [7]. Dynamic control of the amplitude and angle of the internal voltage is utilized to achieve active and reactive power transfer. However, the primary control of P-θ and Q-U becomes challenging due to the coupling between P and Q loops. This coupling becomes more severe as the resistance-to-reactance ratio of the grid impedance and the power angle between the inverter and the grid voltages are increased [26]. Therefore, the AC-side inductance is supposed to be designed considering the ability to decrease the coupling of active and reactive power. On the other hand, in ISynC-based GFM inverter [18], [22], [27] the intrinsic dynamic of the DC-link capacitor is utilized to achieve grid-synchronization. Since the DC capacitor equation is analogous to the rotor motion equation of synchronous generators, the relation between the voltage of DC capacitor and the grid frequency can be matched. However, the AC-side inductance may play a pivotal role in facilitating the DC voltage's ability to perceive fluctuations within the AC grid frequency, which has thus far been unexplored.

Therefore, the objective of this study is to identify optimal AC-side inductance values that contribute to enhancing the performance of GFM inverters across a range of operating conditions and applications. The proposed approach aims to attain optimal performance across multiple metrics, thereby ensuring balanced and efficient inverter operation of different GFM-based inverters. The key contributions of this paper are outlined as follows:

1) Building upon existing AC-side inductance design methods for GFL-based grid-connected inverters, this paper presents an optimized parameter design approach for the AC-side inductance of GFM-based grid-connected inverters, taking into account the specific requirements of diverse applications.

2) For VSG-based GFM inverters, an optimization objective that emphasizes the decoupling capability between active and reactive power is proposed for the design of the AC-side inductance.

3) For ISynC-based GFM inverters, an optimized approach is explored for the design of the AC-side inductance, wherein priority is given to the DC voltage's capability to track fluctuations in the AC grid frequency, while ensuring that it remains unaffected by power or voltage fluctuations.

The remainder of this paper is organized as follows: Section II presents the modeling and control of two distinct types of GFM inverters. Section III proposes the general design methodology and optimized approach for AC-side inductance. Sections IV and V present simulation and experimental results respectively, to validate the theoretical assertions. Finally, Section VI concludes the paper with a summary of key findings.

II. CONTROL OF THE GFM INVERTER

A. Active Power-Based Synchronization Control

Active power synchronization control-based methods can mainly be classified into VSG, PSC, and droop control. The PSC and the basic droop control are equivalent to each other, and they can be categorized as the first-order power control, as shown in Fig. 1. The so-called "virtual inertia" can be synthesized by adding the low-pass filter into the basic droop control, which has been proven equivalent to the VSG control. In this paper, the VSG-based GFM is used as the representation of the PSC and droop control to design the AC-side inductance. Active and reactive power of VSG-based GFM inverters are regulated to ensure the synchronization between the internal voltage U_{vsc} and the grid voltage. The active power and reactive power control loops are used to produce the synchronous rotation angle θ and the d-axis modulation voltage $U_{d\mathrm{ref}}$, respectively. J, K, D_{p} and D_{q} are the virtual inertia, reactive power control coefficient, frequency-drooping and voltage-drooping coefficients of the VSG control, respectively. s is Laplace operator. ω_0 is the reference of the grid angular frequency, i.e., 100π rad/s.

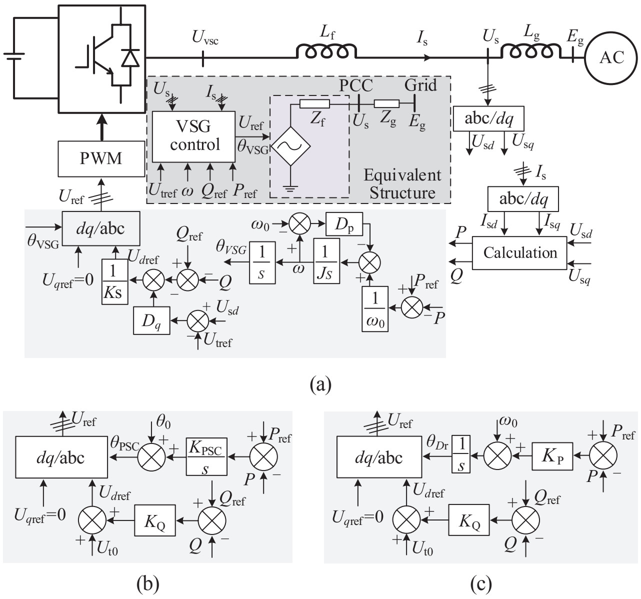

(a)

(b) (c)

Fig. 1. Structure diagram of the active PSC-based GFM inverter. (a) VSG control, (b) PSC control, (c) Droop control.

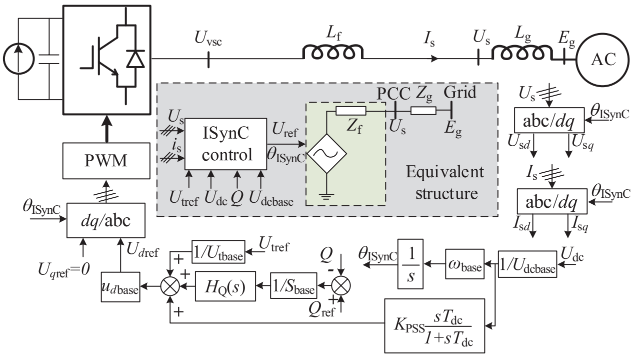

Fig. 2. Structure diagram of the ISynC-based GFM inverter.

B. Inertia Synchronization Control (ISynC)

The structure diagram of the ISynC control is shown in Fig. 2, where the per-unit DC voltage $U_{\mathrm{dc}}/U_{\mathrm{dcbase}}$ is used as the per-unit frequency $\omega/\omega_{\mathrm{base}}$ of the AC-side output voltage. Therefore, the

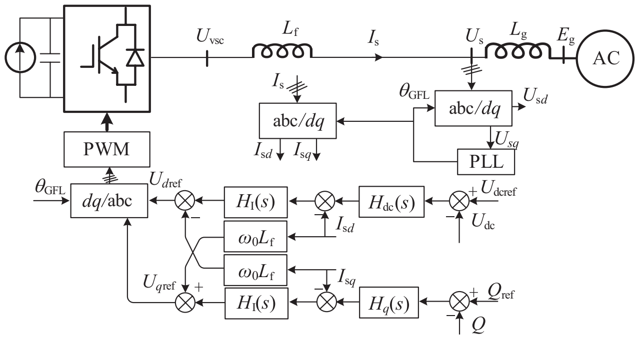

Fig. 3. Structure diagram of a GFL-based grid-connected inverter.

synchronous rotation angle θ_{ISynC} is generated by integrating the per-unit DC voltage. The reactive power Q is regulated by adjusting the amplitude of the modulation voltage. Besides, an auxiliary stabilization control loop comprising a high-pass filter and a gain K_{PSS} is adopted to optimize the inertial response effect.

III. OPTIMIZED DESIGN OF THE AC-SIDE INDUCTANCE OF GFM INVERTERS

A. General Design Method of the AC-Side Inductance

The current design methods of the AC-side inductance are mainly for GFL inverters. Fig. 3 shows the basic structure diagram of GFL control of a grid-connected inverter. The synchronous rotation angle θ_{GFL} is generated by the phase-locked loop (PLL). The general design method for AC-side inductance of GFL inverters is based on the objectives of harmonic attenuation and four-quadrant operation. The upper limit of the AC-side inductance is determined by the requirement of four-quadrant operation, while the lower limit is determined by the requirement of harmonic attenuation [14]–[16].

1) Harmonic attenuation capability. The effective value of the nth harmonic current $I_a(n)$ of inverter is defined in (1), where $U_{ab}(n)$ represents the effective value of the nth harmonic voltage and ω_n signifies the nth harmonic angular frequency. Combining with the total harmonic distortion THD_i of current and (1), the THD_i of inverter considering the AC-side inductance L_f is expressed as (2). I_1 is the effective value of fundamental-frequency current, while I_n denotes the effective value of the nth harmonic current. To ensure that the THD_i of current meets the minimum requirement of $\delta\%$ ($THD_i \leqslant \delta\%$), the inductance L_f should be subjected to (3).

$$I_a(n) = \frac{u_{ab}(n)}{\omega_n L_f} \tag{1}$$

$$THD_i = \frac{1}{I_1}\left(\sum_{n=2,3\cdots}^{\infty} I_n^2\right)^{\frac{1}{2}} = \frac{1}{I_1 L_f}\left[\sum_{n=2,3\cdots}^{\infty} \frac{U_{ab}^2(n)}{\omega_n^2}\right]^{\frac{1}{2}} \tag{2}$$

$$L_{f\_min1} \geqslant \frac{1}{I_1 \delta\%}\left[\sum_{n=2,3\cdots}^{\infty} \frac{U_{ab}^2(n)}{\omega_n^2}\right]^{\frac{1}{2}} \tag{3}$$

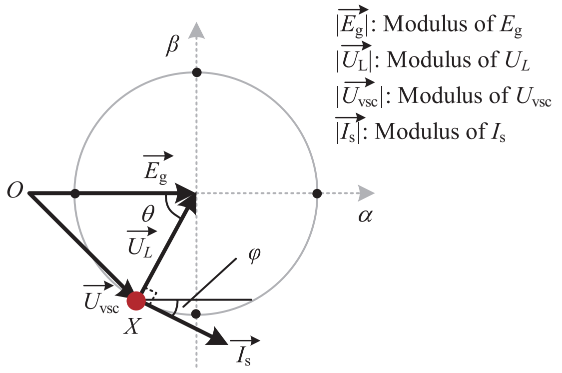

Fig. 4. Steady-state vector diagram of grid-connected inverter in AC side.

2) Four-quadrant operating capability. The total inductance should not be too large because with the increase of the total inductance, the power factor will be reduced, and the voltage drop on the inductor will increase, which will affect the power transmission capacity of the inverter [13]. Thus, there is an upper limit constraint on the total AC-side inductance of the inverter, which is expressed as (4). In (4), U_{dc} is the DC-side voltage, ω_{base} is the fundamental angular frequency, U_{peak} and I_{peak} are the peak values of the phase voltage and current. L_g is the inductance of the AC grid.

$$L_{fmax} + L_g \leqslant \frac{\sqrt{\dfrac{U_{dc}^2}{4} - U_{peak}^2}}{\omega_{base} I_{peak}} \tag{4}$$

During weak and faulty grid conditions, the synchronization instability will be inevitable when the inverter violates the maximum power transfer limit between its terminal bus and the grid. This limitation is present for any control structure [2]. Furthermore, it is important to note that the power flow direction also influences the stable operating area. Generally, the inverters must have four-quadrant operating capability.

Ignoring the impedance of the AC grid, the vector diagram of grid-connected inverter is illustrated in Fig. 4. Under the conditions of a constant voltage vector of AC grid $\left|\overrightarrow{E_g}\right|$ and a constant AC phase current vector $\left|\overrightarrow{I_s}\right|$, four-quadrant operation of grid-connected inverter can be achieved by controlling the amplitude and phase angle of the AC phase voltage vector $\overrightarrow{U_{vsc}}$. The trajectory of the vector $\overrightarrow{U_{vsc}}$ endpoint follows a circle with a radius of $\left|\overrightarrow{U_{vsc}}\right|$ centered at the origin.

To achieve the four-quadrant operation [16]–[19], the point X must be capable of occupying any point along the circular trajectory. Therefore, it is essential to ensure that grid-connected inverter can produce a sufficiently large $\left|\overrightarrow{U_{vsc}}\right|$. However, due to the limitation posed by $\left|\overrightarrow{U_{vsc}}\right|$ in (6) (M and U_{dc} are the modulation index and DC voltage, respectively, $M = 1/2$.), it is crucial to utilize the AC-side inductance to constrain the phase voltage vector of the inductor $\left|\overrightarrow{U_L}\right|$, which is expressed as (7). Thus, combining with the constraint of (5)–(7), the upper limit of L_f

should satisfy (8) to realize the four-quadrant operating capability.

$$\begin{aligned}\left|\overrightarrow{U_{\mathrm{usc}}}\right|^2 &= \left|\overrightarrow{E_{\mathrm{g}}}\right|^2 + \left|\overrightarrow{U_L}\right|^2 - 2\left|\overrightarrow{E_{\mathrm{g}}}\right|\left|\overrightarrow{U_L}\right|\cos\theta \\ &= \left|\overrightarrow{E_{\mathrm{g}}}\right|^2 + \left|\overrightarrow{U_L}\right|^2 - 2\left|\overrightarrow{E_{\mathrm{g}}}\right|\left|\overrightarrow{U_L}\right|\sin\varphi \end{aligned} \quad (5)$$

$$U_{\mathrm{m}} = \left|\overrightarrow{U_{\mathrm{usc}}}\right|^2 \leqslant MU_{\mathrm{dc}} \quad (6)$$

$$\left|\overrightarrow{U_L}\right| = \omega_0 L_{\mathrm{f}}\left|\overrightarrow{I_{\mathrm{s}}}\right| \quad (7)$$

$$L_{\mathrm{f}} \leqslant \frac{\left|\overrightarrow{E_{\mathrm{g}}}\right|\sin\varphi + \sqrt{\left|\overrightarrow{E_{\mathrm{g}}}\right|^2\sin^2\varphi + M^2U_{\mathrm{dc}}^2 - \left|\overrightarrow{E_{\mathrm{g}}}\right|^2}}{\omega_0\left|\overrightarrow{I_{\mathrm{s}}}\right|} \quad (8)$$

Taking into account the static power transfer limitation value P_{PTL} as shown in (9), the upper limit of $L_{\mathrm{f}P}$ can be expressed as (10) by combining with (8) and (9).

$$P_{\mathrm{PTL}} = 1.5\left|\overrightarrow{E_{\mathrm{g}}}\right|\left|\overrightarrow{I_{\mathrm{s}}}\right|\cos\varphi \quad (9)$$

$$L_{\mathrm{f}P} \leqslant \frac{\left|\overrightarrow{E_{\mathrm{g}}}\right|^2\sin\varphi\cos\varphi + \left|\overrightarrow{E_{\mathrm{g}}}\right|\cos\varphi\sqrt{\left|\overrightarrow{E_{\mathrm{g}}}\right|^2\sin^2\varphi + \frac{1}{2}U_{\mathrm{dc}}^2 - \left|\overrightarrow{E_{\mathrm{g}}}\right|^2}}{2P_{\mathrm{PTL}}\omega_0/3} \quad (10)$$

Considering the limitation of reactive power transmission level as shown in (11), the upper limit of $L_{\mathrm{f}Q}$ can be expressed as (12) by combining with (8) and (11).

$$Q = 1.5\left|\overrightarrow{E_{\mathrm{g}}}\right|\left|\overrightarrow{I_{\mathrm{s}}}\right|\sin\varphi \quad (11)$$

$$L_{\mathrm{f}Q} \leqslant \frac{\left|\overrightarrow{E_{\mathrm{g}}}\right|^2\sin\varphi + \left|\overrightarrow{E_{\mathrm{g}}}\right|\sin\varphi\sqrt{\left|\overrightarrow{E_{\mathrm{g}}}\right|^2\sin^2\varphi + \frac{1}{4}U_{\mathrm{dc}}^2 - \left|\overrightarrow{E_{\mathrm{g}}}\right|^2}}{2Q\omega_0/3} \quad (12)$$

B. Optimized Design of the AC-Side Inductance for VSG-Based Inverters

Active and reactive power coupling of single grid-connected inverter results from the interactions among slower control loops that regulate the phasor quantities such as active and reactive power, as well as the amplitude and frequency of the voltages at the PCC. It is more insightful to represent the dynamics of the inverters in terms of these phasor quantities rather than phase variables including three-phase voltages and currents [28]. This follows the same logic of using active and reactive power flows as well as the frequency, angle, and magnitude of voltages as state variables for analyzing the stability of power systems [29]. Therefore, this paper employs admittance/impedance transfer functions in terms of phasor quantities for power coupling analysis, which is known as the power-domain admittance model (PDAM) or power-domain impedance model (PDIM) [28]. This approach follows the same logic as using active and reactive power flows, as well as the frequency, angle, and amplitude of bus voltages, as state variables for analyzing the characteristics of bulk power systems [29]. The equivalent circuit of GFM inverter and its phasor diagram are shown in Fig. 5.

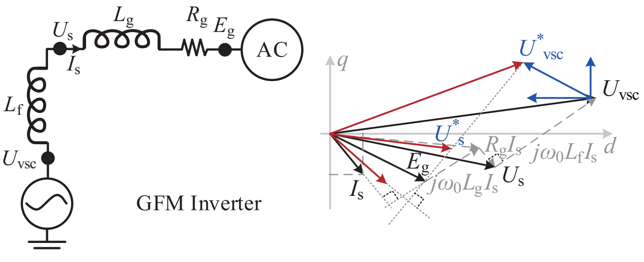

(a) (b)

Fig. 5. GFM inverter and its phasor diagram. (a) Equivalent circuit, (b) Phasor diagram.

As shown in (13), small disturbance in the *d*-/*q*-components of voltages can be related with the small disturbance in the amplitude $\Delta U_{\mathrm{M}}(s)$ and frequency $\Delta F_{\mathrm{M}}(s)$ of voltages U_{s} at the PCC, where U_0 is the amplitude of the voltage U_{s}. The variables with "Δ" represent small disturbance. Note that the Laplace variable $s(s = j\omega_{\mathrm{p}})$ represents the complex perturbation frequency. The relation between $\Delta U_{sq}(s)$ and $\Delta\theta(s)$ follows from the fact that the small disturbance in *q*-axis voltage is directly proportional to the perturbation in the phase of the PCC voltages, the latter can be related with the perturbation in the frequency $\Delta F_{\mathrm{M}}(s)$ of the PCC voltages [30].

$$\begin{bmatrix}\Delta U_{sd}(s)\\ \Delta U_{sq}(s)\end{bmatrix} = \begin{bmatrix}G_{\mathrm{U}_d\mathrm{F}_\mathrm{M}}(s) & G_{\mathrm{U}_d\mathrm{U}_\mathrm{M}}(s)\\ G_{\mathrm{U}_q\mathrm{F}_\mathrm{M}}(s) & G_{\mathrm{U}_q\mathrm{U}_\mathrm{M}}(s)\end{bmatrix} \cdot \begin{bmatrix}\Delta F_{\mathrm{M}}(s)\\ \Delta U_{\mathrm{M}}(s)\end{bmatrix} \quad (13)$$

where $G_{U_dF_{\mathrm{M}}}(s) = 0$, $G_{U_dU_{\mathrm{M}}}(s) = 1$, $G_{U_qF_{\mathrm{M}}}(s) = \frac{2\pi U_0}{s}$, and $G_{U_qU_{\mathrm{M}}}(s) = 0$.

The instantaneous active and reactive power inputs to the grid can be linearized (14). U_{d0} and U_{q0} are the steady-state value of *d*-/*q*-axis voltage in PCC. I_{d0} and I_{q0} represent the steady-state values of the *d*-/*q*-axis current.

$$\begin{bmatrix}\Delta P(s)\\ \Delta Q(s)\end{bmatrix} = \frac{3}{2}\begin{bmatrix}U_{d0} & U_{q0}\\ U_{q0} & -U_{d0}\end{bmatrix} \cdot \begin{bmatrix}\Delta I_{sd}(s)\\ \Delta I_{sq}(s)\end{bmatrix} + \frac{3}{2}\begin{bmatrix}I_{d0} & I_{q0}\\ -I_{q0} & I_{d0}\end{bmatrix} \cdot \begin{bmatrix}\Delta U_{sd}(s)\\ \Delta U_{sq}(s)\end{bmatrix} \quad (14)$$

If the small disturbance of frequency is assumed to be much smaller than the fundamental frequency, the small disturbance in $\Delta I_{sd}(s)$, $\Delta I_{sq}(s)$, $\Delta U_{sd}(s)$, and $\Delta U_{sq}(s)$ can be related depending on the grid impedance, which is expressed as (15). $\Delta I_{sd}(s)$ and $\Delta I_{sq}(s)$ can also be expressed as (16) by considering the dynamic of the VSG-based GFM inverter.

$$\begin{bmatrix}\Delta U_{sd}(s)\\ \Delta U_{sq}(s)\end{bmatrix} = \begin{bmatrix}R_{\mathrm{g}} & -\omega_0 L_{\mathrm{g}}\\ \omega_0 L_{\mathrm{g}} & R_{\mathrm{g}}\end{bmatrix} \cdot \begin{bmatrix}\Delta I_{sd}(s)\\ \Delta I_{sq}(s)\end{bmatrix} \quad (15)$$

$$\begin{bmatrix}\Delta I_{sd}(s)\\ \Delta I_{sq}(s)\end{bmatrix} = \begin{bmatrix}\dfrac{R_{\mathrm{g}}}{\omega_0^2(L_{\mathrm{g}}+L_{\mathrm{f}})^2+R_{\mathrm{g}}^2} & \dfrac{\omega_0(L_{\mathrm{g}}+L_{\mathrm{f}})}{\omega_0^2(L_{\mathrm{g}}+L_{\mathrm{f}})^2+R_{\mathrm{g}}^2}\\ -\dfrac{\omega_0(L_{\mathrm{g}}+L_{\mathrm{f}})}{\omega_0^2(L_{\mathrm{g}}+L_{\mathrm{f}})^2+R_{\mathrm{g}}^2} & \dfrac{R_{\mathrm{g}}}{\omega_0^2(L_{\mathrm{g}}+L_{\mathrm{f}})^2+R_{\mathrm{g}}^2}\end{bmatrix} \cdot \begin{bmatrix}\Delta U_{\mathrm{usc}d}(s)\\ \Delta U_{\mathrm{usc}q}(s)\end{bmatrix} \quad (16)$$

$$\begin{bmatrix}\Delta U_{\mathrm{usc}d}(s)\\ \Delta U_{\mathrm{usc}q}(s)\end{bmatrix} = \begin{bmatrix}0 & 1\\ \dfrac{2\pi V_0}{s} & 0\end{bmatrix}\cdot\begin{bmatrix}\Delta F_{\mathrm{M}}(s)\\ \Delta U_{\mathrm{M}}(s)\end{bmatrix} \tag{17}$$

Combining with (14)–(17), PDIM of the GFM inverter can be obtained as (18). $\Delta P(s)$ and $\Delta Q(s)$ represent small disturbance in the active and reactive power, respectively.

$$\begin{bmatrix}\Delta F_{\mathrm{M}}(s)\\ \Delta U_{\mathrm{M}}(s)\end{bmatrix} = \begin{bmatrix}Z_{\mathrm{FP}}(s) & Z_{\mathrm{FQ}}(s)\\ Z_{\mathrm{UP}}(s) & Z_{\mathrm{UQ}}(s)\end{bmatrix}\cdot\begin{bmatrix}\Delta P(s)\\ \Delta Q(s)\end{bmatrix} \tag{18}$$

$$Z_{\mathrm{FP}}(s) = \frac{(-V_{d0}L_{\mathrm{g}} - V_{d0}L_{\mathrm{f}} + I_{d0}R_{\mathrm{g}}L_{\mathrm{f}})\omega_0 s}{2\pi V(1.5I_{d0}^2L_{\mathrm{g}}^2\omega_0^2 + 1.5I_{d0}^2R_{\mathrm{g}}^2 - 1.5V_{d0}^2)} \tag{19}$$

$$Z_{\mathrm{UP}}(s) = \frac{I_{d0}\omega_0^2L_{\mathrm{g}}L_{\mathrm{f}} + I_{d0}\omega_0^2L_{\mathrm{g}}^2 + I_{d0}R_{\mathrm{g}}^2 - R_{\mathrm{g}}V_{d0}}{1.5I_{d0}^2L_{\mathrm{g}}^2\omega_0^2 + 1.5I_{d0}^2R_{\mathrm{g}}^2 - 1.5V_{d0}^2} \tag{20}$$

$$Z_{\mathrm{FQ}}(s) = \frac{(R_{\mathrm{g}}V_{d0} + I_{d0}R_{\mathrm{g}}^2 + I_{d0}\omega_0^2L_{\mathrm{g}}L_{\mathrm{f}} + I_{d0}\omega_0^2L_{\mathrm{g}}^2)s}{2\pi V(1.5I_{d0}^2L_{\mathrm{g}}^2\omega_0^2 + 1.5I_{d0}^2R_{\mathrm{g}}^2 - 1.5V_{d0}^2)} \tag{21}$$

$$Z_{\mathrm{UQ}}(s) = -\frac{(I_{d0}R_{\mathrm{g}}L_{\mathrm{f}} + V_{d0}L_{\mathrm{f}} + V_{d0}L_{\mathrm{g}})\omega_0}{1.5I_{d0}^2L_{\mathrm{g}}^2\omega_0^2 + 1.5I_{d0}^2R_{\mathrm{g}}^2 - 1.5V_{d0}^2} \tag{22}$$

Dynamic relative gain array (DRGA) is used to quantify the degree of coupling between active and reactive power [24]. DRGA of the studied system is defined as $\boldsymbol{\Lambda}_{\mathbf{PQ}}(s)$, where the matrix $\boldsymbol{\Lambda}_{\mathbf{PQ}}(s)$ is composed of dynamic relative gains $\lambda_{ij}(s)$. It is noted that DRGA can be transfer to RGA if s is 0.

$$\begin{aligned}\boldsymbol{\Lambda}_{\mathbf{PQ}}(s) = &\begin{bmatrix}Z_{\mathrm{FP}}(s) & Z_{\mathrm{FQ}}(s)\\ Z_{\mathrm{UP}}(s) & Z_{\mathrm{UQ}}(s)\end{bmatrix} \otimes \left(\begin{bmatrix}Z_{\mathrm{FP}}(s) & Z_{\mathrm{FQ}}(s)\\ Z_{\mathrm{UP}}(s) & Z_{\mathrm{UQ}}(s)\end{bmatrix}^{-1}\right)^{\mathrm{T}}\\ &\begin{bmatrix}\lambda_{11}(s) & \lambda_{12}(s)\\ \lambda_{21}(s) & \lambda_{22}(s)\end{bmatrix}\end{aligned} \tag{23}$$

In (23), $\otimes$ represents Hadamard product. $\lambda_{11}(s)$ and $\lambda_{22}(s)$ are expressed as (24), $\lambda_{12}(s) = \lambda_{21}(s) = 1 - \lambda_{11}(s)$. The power coupling degree can be minimized by approaching the DRGA to the identity matrix, where the diagonal elements approximate 1 at various frequencies and the off-diagonal elements approach 0 ($\lambda_{11}(s) \approx 1, \lambda_{12}(s) \approx 0$).

$$\lambda_{11}(s) = \lambda_{22}(s) = \left[1 - \frac{Z_{\mathrm{UP}}(s)Z_{\mathrm{FQ}}(s)}{Z_{\mathrm{FP}}(s)Z_{\mathrm{UQ}}(s)}\right]^{-1} \tag{24}$$

On this basis, the relative coupling coefficient $DR_{\mathrm{PQ}}(s)$ is defined to quantitatively analyze the coupling characteristics. The calculation formula of the relative coupling coefficient $DR_{\mathrm{PQ}}(s)$ is expressed as (25). $\boldsymbol{\Lambda}_{\mathbf{PQ}}(s)$ is the system dynamic relative gain matrix, $\boldsymbol{I}$ is the 2×2 identity matrix, "sum" is the matrix summation norm. The amplitude of the $DR_{\mathrm{PQ}}(s)$ provides an intuitive metric of power coupling degree [31].

$$DR_{\mathrm{PQ}}(s) = \frac{\left\| \boldsymbol{\Lambda}_{\mathbf{FQ}}(s) - \boldsymbol{I} \right\|_{\mathrm{sum}}}{4} \tag{25}$$

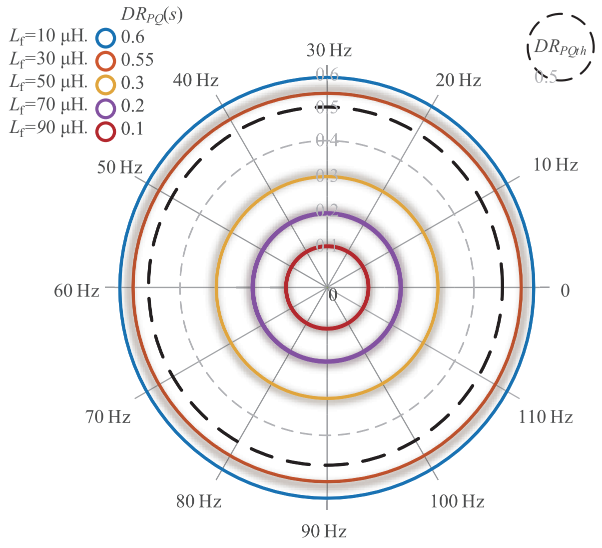

Fig. 6. Power coupling diagram with different filter inductance.

When $DR_{\mathrm{PQ}}(s)$ is close to 0, the power coupling can be negligible; if the $DR_{\mathrm{PQ}}(s)$ exceeds 0.5 [24], it indicates a significant power coupling degree within the system and a more severe degree of power coupling with a higher $DR_{\mathrm{PQ}}(s)$. Power coupling will be decreased with increasing the AC-side inductance of VSG-based inverter. Therefore, lower limitation of the AC-side inductance can be obtained according to the power coupling threshold, as shown in Fig. 6. In Fig. 6, the circles with different colors depict the power coupling degree of VSG-based inverters with different AC-side inductance values across varying frequency ranges. According to (18) and (25), the power coupling arising from variations in the AC-side inductance remains consistent across all frequency ranges. The decrease of the AC-side inductance results in the increase of the circle area, thereby leading to greater power coupling. The black dashed line signifies the critical threshold for power coupling. If the circle area exceeds the critical threshold, the system becomes susceptible to instability. Consequently, the lower limitation of the AC-side inductance can be designed based on the minimum threshold for power coupling.

C. Optimized Design of the AC-Side Inductance for ISynC-Based Inverters

For ISynC-based inverters, DC voltage is needed to real-time sense the changes in grid frequency. The DC voltage is required not to exceed a limited amplitude if the active power or AC grid voltage changes. Therefore, the AC-side inductance of ISynC-based inverters can be optimized based on the relationship between DC voltage fluctuation ΔU_{dc} and grid frequency fluctuation $\Delta\omega_{\mathrm{g}}$, active power fluctuation ΔP_{r}, or grid voltage fluctuation ΔE_{g} in this section.

Ignoring the power loss of ISynC-based inverter, the output power P_{r} is expressed as (26) according to [22], in which U_{vsc} is the output voltage, E_{g} is the grid voltage, and δ is the phase difference between the inverter voltage and grid voltage, which is expressed as (27). Additionally, ω_{g} is the grid angular frequency. X_{total} represents the total reactance, that is $\omega_0(L_{\text{f}}+L_{\text{g}})$.

$$P_{\text{r}}=\frac{U_{\text{dc}}U_{\text{vsc}}E_{\text{g}}}{X_{\text{total}}}\sin\delta=\frac{U_{\text{dc}}U_{\text{vsc}}E_{\text{g}}}{\omega_0(L_{\text{f}}+L_{\text{g}})}\sin\delta \tag{26}$$

$$\delta=\frac{\omega_0}{s}(U_{\text{dc}}-\omega_{\text{g}}) \tag{27}$$

1) AC-side inductance optimized design based on the relationship between DC voltage fluctuation and grid frequency fluctuation. When ω_{g} fluctuates but E_{g} remains constant, P_{r} can be linearized as (28). U_{dc0}, U_{vsc0}, E_{g0}, and δ_0 denote the steady-state values.

$$\Delta P_{\text{r}}=\frac{U_{\text{dc0}}U_{\text{vsc0}}E_{\text{g0}}}{\omega_0(L_{\text{f}}+L_{\text{g}})}\cos\delta_0\Delta\delta+\frac{U_{\text{dc0}}E_{\text{g0}}}{\omega_0(L_{\text{f}}+L_{\text{g}})}\sin\delta_0\Delta U_{\text{vsc}}+\frac{U_{\text{vsc0}}E_{\text{g0}}}{\omega_0(L_{\text{f}}+L_{\text{g}})}\sin\delta_0\Delta U_{\text{dc}} \tag{28}$$

For ISynC-based GFM inverters, the DC voltage should autonomously sense the grid frequency fluctuation. Therefore, the relationship between the DC voltage variation and the grid frequency fluctuation is expressed as (29). $G_{\text{dc}\_\omega}(s)$ is expressed as (30). HC is the inertia time constant of the DC capacitor.

$$\Delta U_{\text{dc}}=G_{\text{dc}\_\omega}(s)\cdot\Delta\omega_{\text{g}} \tag{29}$$

$$G_{\text{dc}\_\omega}(s)=\frac{U_{\text{dc0}}U_{\text{vsc0}}E_{\text{g0}}\omega_0\cos\delta_0}{2\omega_0(L_{\text{f}}+L_{\text{g}})H_{\text{C}}s^2+U_{\text{vsc0}}E_{\text{g0}}\omega_0\sin\delta_0 s+U_{\text{dc0}}U_{\text{vsc0}}E_{\text{g0}}\omega_0\cos\delta_0} \tag{30}$$

To assure the DC voltage variation does not exceed the threshold $\Delta U_{\text{dc}\_\text{th}\omega}$, the maximum of the $G_{\text{dc}\_\omega}(s)$ should meet the relationship as shown in (31).

$$\max[G_{\text{dc}\_\omega}(s)]=\left[\frac{4U_{\text{dc0}}U_{\text{vsc0}}E_{\text{g0}}\cos\delta_0\omega_0^2(L_{\text{f}}+L_{\text{g}})}{\sqrt{-(U_{\text{vsc0}}E_{\text{g0}}\sin\delta_0)^4+8\sin^2\delta_0H_{\text{C}}U_{\text{dc0}}U_{\text{vsc0}}^3E_{\text{g0}}^3\cos\delta_0\omega_0^2(L_{\text{f}}+L_{\text{g}})}}\right]\leqslant|\Delta U_{\text{dc}\_\text{th}\omega}|/|\Delta\omega_{\text{g}}| \tag{31}$$

Thus, the upper and lower limits of the AC-side inductance can be obtained, which are expressed as (32) and (33).

$$L_{\text{f}\_\max\_U_{\text{dc}}\_\omega}\leqslant\frac{\sin\delta_0\left[1+\sqrt{1-\left(\frac{|\Delta U_{\text{dc}\_\text{th}\omega}|}{|\Delta\omega_0|}\right)^2\left(\frac{U_{\text{vsc0}}E_{\text{g0}}\omega_0\sin\delta_0}{2H_{\text{C}}}\right)^2}\right]}{50\pi\left(\frac{|\Delta U_{\text{dc}\_\text{th}\omega}|}{|\Delta\omega_0|}\right)^2U_{\text{dc0}}\omega_0\cos\delta_0}-L_{\text{g}} \tag{32}$$

$$L_{\text{f}\_\max\_U_{\text{dc}}\_\omega}\leqslant\frac{\sin\delta_0\left[1-\sqrt{1-\left(\frac{|\Delta U_{\text{dc}\_\text{th}\omega}|}{|\Delta\omega_0|}\right)^2\left(\frac{U_{\text{vsc0}}E_{\text{g0}}\omega_0\sin\delta_0}{2H_{\text{C}}}\right)^2}\right]}{50\pi\left(\frac{|\Delta U_{\text{dc}\_\text{th}\omega}|}{|\Delta\omega_0|}\right)^2U_{\text{dc0}}\omega_0\cos\delta_0}-L_{\text{g}} \tag{33}$$

2) AC-side inductance optimized design based on the relationship between DC voltage fluctuation and grid voltage fluctuation. When grid voltage fluctuates but grid frequency remains constant, active power P_{r} can be linearized as (34). Based on (26) and (27), the relationship between the DC voltage variation and the grid voltage fluctuation is expressed as (35). $G_{\text{dc}\_E}(s)$ is expressed as (36).

$$\Delta P_{\text{r}}=\frac{U_{\text{dc0}}U_{\text{vsc0}}E_{\text{g0}}}{\omega_0(L_{\text{f}}+L_{\text{g}})}\cos\delta_0\Delta\delta+\frac{U_{\text{dc0}}E_{\text{g0}}}{\omega_0(L_{\text{f}}+L_{\text{g}})}\sin\delta_0\Delta U_{\text{vsc}}-\frac{U_{\text{dc0}}E_{\text{vsc0}}}{\omega_0(L_{\text{f}}+L_{\text{g}})}\sin\delta_0\Delta E_{\text{g}}+\frac{U_{\text{vsc0}}E_{\text{g0}}}{\omega_0(L_{\text{f}}+L_{\text{g}})}\sin\delta_0\Delta U_{\text{dc}} \tag{34}$$

$$\Delta U_{\text{dc}}=G_{\text{dc}\_E}(s)\cdot\Delta E_{\text{g}} \tag{35}$$

$$G_{\text{dc}\_E}(s)=\frac{\dfrac{U_{\text{dc0}}U_{\text{vsc0}}\sin\delta_0}{2\omega_0(L_{\text{f}}+L_{\text{g}})H_{\text{C}}}}{s^2+\dfrac{U_{\text{vsc0}}E_{\text{g0}}\sin\delta_0}{2\omega_0(L_{\text{f}}+L_{\text{g}})H_{\text{C}}}s+\dfrac{U_{\text{dc0}}U_{\text{vsc0}}E_{\text{g0}}\omega_0\cos\delta_0}{2\omega_0(L_{\text{f}}+L_{\text{g}})H_{\text{C}}}} \tag{36}$$

The threshold of DC voltage variation is represented by $|\Delta U_{\text{dc}\_\text{th}E}|$, and the AC grid voltage variation is denoted by $|\Delta E_{\text{g}}|$. When ΔE_{g} varies, in order to keep DC voltage fluctuation within its threshold, the relationship between $|\Delta U_{\text{dc}\_\text{th}E}|$ and $|\Delta E_{\text{g}}|$ must be satisfied as (37). The maximum of the G_{dc_E}(s) is expressed as (38).

$$\max[G_{\text{dc}\_E}(s)]\leqslant|\Delta U_{\text{dc}\_\text{th}E}|/|\Delta E_{\text{g}}| \tag{37}$$

$$\max[G_{\text{dc}\_E}(s)]=\max\left[\frac{\dfrac{U_{\text{dc0}}U_{\text{vsc0}}\sin\delta_0}{2\omega_0(L_{\text{f}}+L_{\text{g}})H_{\text{C}}}s}{s^2+\dfrac{U_{\text{vsc0}}E_{\text{g0}}\sin\delta_0}{2\omega_0(L_{\text{f}}+L_{\text{g}})H_{\text{C}}}s+\dfrac{U_{\text{dc0}}U_{\text{vsc0}}E_{\text{g0}}\omega_0\cos\delta_0}{2\omega_0(L_{\text{f}}+L_{\text{g}})H_{\text{C}}}}\right]=\frac{U_{\text{dc0}}U_{\text{vsc0}}\sin\delta_0}{2\omega_0(L_{\text{f}}+L_{\text{g}})H_{\text{C}}} \tag{38}$$

The lower limit of the AC-side inductance can be obtained as (39).

$$L_{\text{f}\_\min\_U_{\text{dc}}\_E}\geqslant\frac{U_{\text{dc0}}U_{\text{vsc0}}\sin\delta_0}{200\pi H_{\text{C}}}\frac{|\Delta E_{\text{g}}|}{|\Delta U_{\text{dc}\_\text{th}E}|}-L_{\text{g}} \tag{39}$$

3) AC-side inductance optimized design based on the relationship between DC voltage fluctuation and active power fluctuation. When the output power P_{r} fluctuates, P_{r} can be linearized as (28). If ω_{g} and E_{g} remain constant, based on (26) and (27), the relationship between the DC voltage variation and the active power fluctuation is expressed as (40). G_{dc_P}(s) is expressed as (41).

$$\Delta U_{\text{dc}}=\text{G}_{\text{dc}\_P}(s)\Delta P_{\text{r}} \tag{40}$$

$$\text{G}_{\text{dc}\_P}(s)=\frac{s/2H_{\text{C}}}{s^2+\dfrac{U_{\text{vsc0}}E_{\text{g0}}\sin\delta_0}{2\omega_0(L_{\text{f}}+L_{\text{g}})H_{\text{C}}}s+\dfrac{U_{\text{dc0}}U_{\text{vsc0}}E_{\text{g0}}\omega_0\cos\delta_0}{2\omega_0(L_{\text{f}}+L_{\text{g}})H_{\text{C}}}} \tag{41}$$

The threshold of DC voltage variation is set as $|\Delta U_{\text{dc}\_\text{th}P}|$. $|\Delta P_{\text{r}}|$ represents the variation of active power of grid. When ΔP_{r} changes, in order to keep ΔU_{dc} not exceed its threshold, the relationship must be satisfied, which is expressed in (42). The maximum of the $G_{\mathrm{dc}\_P}(s)$ is expressed as (43).

$$\max[G_{\mathrm{dc}\_P}(s)] \leqslant |\Delta U_{\mathrm{dc\_th}P}| \,/\, |\Delta P_{\mathrm{r}}| \tag{42}$$

$$\begin{aligned}\max[G_{\mathrm{dc}\_P}(s)] &= \max\left\{\left|\frac{s/2H_{\mathrm{C}}}{s^2+\dfrac{U_{\mathrm{vsc0}}E_{\mathrm{g0}}\sin\delta_0}{2\omega_0(L_{\mathrm{f}}+L_{\mathrm{g}})H_{\mathrm{C}}}s+\dfrac{U_{\mathrm{dc0}}U_{\mathrm{vsc0}}E_{\mathrm{g0}}\omega_0\cos\delta_0}{2\omega_0(L_{\mathrm{f}}+L_{\mathrm{g}})H_{\mathrm{C}}}}\right|\right\} \\ &= \frac{\omega_0(L_{\mathrm{f}}+L_{\mathrm{g}})}{U_{\mathrm{vsc0}}E_{\mathrm{g0}}\sin\delta_0}\end{aligned} \tag{43}$$

And the upper limit of the AC-side inductance can be obtained as (44).

$$L_{\mathrm{f\_max}\_U_{\mathrm{dc}}\_P} \leqslant \frac{1}{100\pi}\,\frac{|\Delta U_{\mathrm{dc\_th}P}|}{|\Delta P_{\mathrm{r}}|}\,(U_{\mathrm{vsc0}}E_{\mathrm{g0}}\sin\delta_0) \tag{44}$$

II. CASE STUDY AND SIMULATION RESULTS

A. Optimized Design for AC-Side Inductance

For GFL or GFM inverters, by considering the harmonic mitigating function $f_{\mathrm{THDi}}(x)$ and the four-quadrant operating capability $f_{\mathrm{PQPTL}}(x)$, the constraints of AC-side inductance are formulated as (45) and (46), respectively.

$$\begin{gathered}\min L_{\mathrm{f\_min1}} = f_{\mathrm{THD}_i}(x) \\ \text{s.t.}\quad L_{\mathrm{f\_min1}} \geqslant \frac{1}{I_1\delta\%}\left[\sum_{n=2,3\cdots}^{\infty}\frac{U_{\mathrm{ab}}^2(n)}{\omega_n^2}\right]^{\frac{1}{2}} \\ \delta\% = \max(1\%, 2\%, \ldots, 5\%, \ldots),\ n^{\mathrm{th}} = 3, 5, 7, 9, \ldots\end{gathered}$$

$$\max L_{\mathrm{f\_max1}} = f_{\mathrm{PQPTL}}(\mathrm{x}) \tag{45}$$

$$\begin{gathered}\text{s.t.}\quad L_{\mathrm{fmax}} \subseteq E\mathrm{q}.4,\ L_{\mathrm{fP}} \subseteq E\mathrm{q}.10,\ L_{\mathrm{fQ}} \subseteq E\mathrm{q}.12. \\ L_{\mathrm{f\_max1}} \leqslant \min\{L_{\mathrm{fmax}}, L_{\mathrm{fP}}, L_{\mathrm{fQ}}\}\end{gathered} \tag{46}$$

For VSG-based inverter, power coupling should be decreased when designing the AC-side inductance and its constraint condition $f_{\mathrm{DRPQ}}(x)$ is expressed as (47).

$$\begin{gathered}\min L_{\mathrm{f\_min2}} = f_{\mathrm{DRPQ}}(x) \\ \text{s.t.}\ L_{\mathrm{f\_min2}} \geqslant L_{\mathrm{f\_VSG\_PQ}},\ L_{\mathrm{f\_VSG\_PQ}} \propto f_{\mathrm{DRPQth}}(x)\end{gathered} \tag{47}$$

By considering the anti-disturbance capability of ISynC-based GFM inverter, the corresponding constraint condition is expressed in (48). If DC voltage of the ISynC-based inverter is capable of accurately sensing grid frequency fluctuations, it means $|\Delta U_{\mathrm{dc\_th}\omega}| / |\Delta\omega_{\mathrm{g}}| \approx 1$, $|\Delta U_{\mathrm{dc\_th}P}| / |\Delta P_{\mathrm{r}}| \approx 0$, and $|\Delta U_{\mathrm{dc\_th}E}| / |\Delta E_{\mathrm{g}}| \approx 0$.

$$\begin{aligned}&\min/\max L_{\mathrm{ISynC}} = f_{\mathrm{ISynC}}(x) \\ &\quad= \left\{\max\frac{|\Delta U_{\mathrm{dc\_th}\omega}|}{|\Delta\omega_{\mathrm{g}}|},\ \min\frac{|\Delta U_{\mathrm{dc\_th}E}|}{|\Delta E_{\mathrm{g}}|},\ \min\frac{|\Delta U_{\mathrm{dc\_th}P}|}{|\Delta P_{\mathrm{r}}|}\right\} \\ &\text{s.t.}\quad \mathrm{Eq}.32,\ \mathrm{Eq}.33,\ \mathrm{Eq}.39,\ \mathrm{Eq}.44.\end{aligned} \tag{48}$$

TABLE I
PARAMETERS OF THE INVERTER

Parameters	Value
Rated power/MW	4.5
AC voltage/V	564
DC voltage/V	1200
DC capacitance/μF	10000
AC grid resistance/Ω	0.02
AC grid inductance/μH	50

TABLE II
PARAMETERS DESIGN FOR SUPPRESSING THE HARMONIC

Harmonic total order	Upper limitation of THD/%	Min *Lf* /μH
9	1	81.402
	2	40.701
	3	27.134
	4	20.351
	5	16.280

For GFM-based inverters, the optimization can be expressed as (49). Weights factors γ_i can be set to choose one of the optimal solutions as the design parameters according to the degree of preference for different parameters optimization of GFM-based inverters. $i = 1, 2, 3, 4$. For example, $\gamma_1 + \gamma_2 = 1$ and $\gamma_3 = \gamma_4 = 0$ if the traditional design method of GFL-based inverter is considered.

$$\begin{gathered}\min/\max F_{\mathrm{Nor}}(x) = \gamma_1 f_{\mathrm{THD}_i}(x) + \gamma_2 f_{\mathrm{PQPTL}}(x) + \gamma_3 f_{\mathrm{DRPQ}}(x) + \gamma_4 f_{\mathrm{ISynC}}(x) \\ \text{s.t.}\quad \gamma_1 + \gamma_2 + \gamma_3 + \gamma_4 = 1\end{gathered} \tag{49}$$

B. Optimal Design Verification for VSG-Based Inverter

Main parameters of VSG-based inverter are shown in Table I.

1) AC-side inductance designed by the traditional method of GFL-based inverter. For VSG-based inverter, if the influence of harmonic suppression function and power transmission limit (i.e., the four-quadrant operating capability) are only considered, weights factors γ_n of (49) are expressed as (50).

$$\gamma_1 + \gamma_2 = 1,\ \text{and}\ \gamma_3 = 0,\ \gamma_4 = 0 \tag{50}$$

The upper limit value of the AC-side inductance determined by power transmission limit considerations stands at 151.71 μH, and the lower limit value determined by harmonic suppression (with the upper limit 5% of THD) is 16.280 μH, as shown in Table II. If the AC-side inductance is set to 20 μH, the power coupling appears in the reactive power when the active power reference changes from 0.7 p.u. to 1.0 p.u. Also, the oscillation appears and presents the convergence trend, as shown in Fig. 7 (a). If the AC-side inductance exceeds the upper limit restrained by the power transmission limit, for instance, 200 μH is selected here, power instability will appear when the active power reference changes from 0.7 p.u. to 1.0 p.u., as shown in Fig. 7 (d). Therefore, if the traditional parameter design method

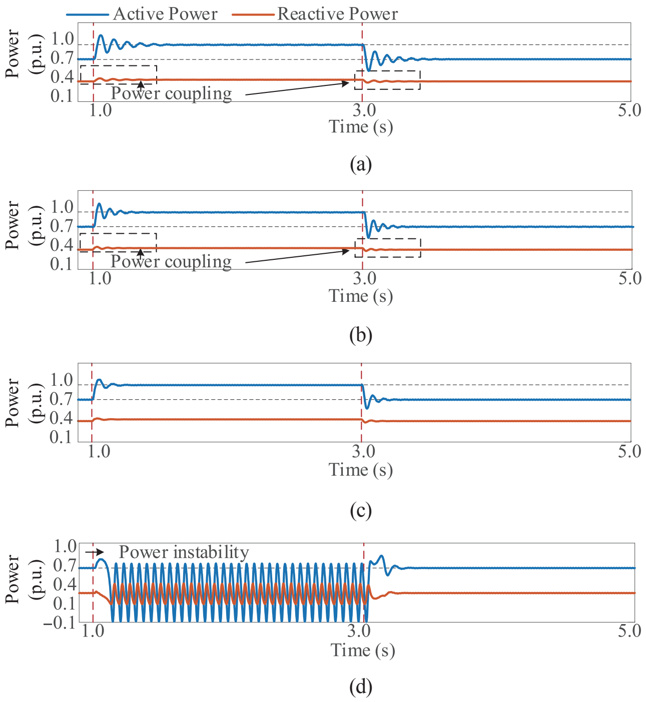

(a)

(b)

(c)

(d)

Fig. 7. Power waveforms when active power changes. (a) $L_f = 20$ μH, (b) $L_f = 50$ μH, (c) $L_f = 100$ μH, (d) $L_f = 200$ μH.

TABLE III

Parameters Design of Inductance for VSG-Based Inverter

μH

Constraint condition	Upper limit	Lower limit
Harmonic suppression function	—	16.280
Power transmission limit	151.71	—
Power decoupling function ($DR_{PQ} = 0.5$)	—	41

for GFL-based inverters is adopted, the lower limit value designed based on THD is not applicable, which will lead to the intensified power coupling and oscillation of VSG-based GFM inverters.

2) AC-side inductance designed by the optimal method. For VSG-based GFM inverter, the upper limit of the power coupling DR_{PQ} is set to 0.5 in this paper. According to optimized design in (47), weights factors γ_n of (49) can be expressed as (51). The parameters optimal results of AC-side inductance for VSG-based inverter can be obtained through (52) and shown in Table III.

$$\gamma_1 + \gamma_2 + \gamma_3 = 1, \text{ and } \gamma_4 = 0 \tag{51}$$

$$\begin{cases} L_{\text{fVSGmax}} = \min\{\text{Eq.4, Eq.10, Eq.12}\} \\ L_{\text{fVSGmin}} = \max\{\text{Eq.3, Eq.47}\} \end{cases} \tag{52}$$

Thus, the lower limit of the AC-side inductance can be optimized as 41 μH. Power coupling is decreased with increasing the AC-side inductance of VSG-based GFM inverter, as shown in Fig. 7(b)–(c). If the AC-side inductance is increased to 50 μH, the power coupling and oscillation can be alleviated compared with that of 20 μH. If the AC-side inductance reaches 100 μH, the oscillation and power coupling can be gradually suppressed, as shown in Fig. 7(c). The upper limit of the AC-side inductance can be designed according to the power transmission limitation.

TABLE IV

Parameters Design of Inductance for ISynC-Based Inverter

μH

Constraint condition	Upper limit	Lower limit
Harmonic suppression function	—	16.280
Power transmission limit	151.71	—
Constraint between DC voltage fluctuation and grid frequency fluctuation	80.833	—
Constraint between DC voltage fluctuation and grid voltage fluctuation	—	12.727
Constraint between DC voltage fluctuation and active power fluctuation	116.47	—

C. Optimal Design Verification for ISynC-Based Inverter

1) Optimal design of parameters for ISynC-based inverter. For ISynC-based inverter, weights factors γ_n of (49) can be expressed as (53). Power coupling is not considered due to its own control objective of ISynC-based inverter. Main parameters are the same as VSG-based inverter. The parameters optimal results of AC-side inductance for ISynC-based inverter can be obtained through (54) and shown in Table IV. The optimized design of the ISynC-based inverter yields an AC-side inductance range, with an upper limit of 80.833 μH and a lower limit of 16.280 μH.

$$\gamma_1 + \gamma_2 + \gamma_4 = 1, \text{ and } \gamma_3 = 0 \tag{53}$$

$$\begin{cases} L_{\text{fISynCmax}} = \min\{\text{Eq.4, Eq.10, Eq.12, Eq.32, Eq.44}\} \\ L_{\text{fISynCmin}} = \max\{\text{Eq.3, Eq.33, Eq.39}\} \end{cases} \tag{54}$$

2) Comparison with the AC-side inductance designed by the traditional method of GFL-based inverter. To demonstrate the effect of the AC-side inductance optimization, an artificial grid's frequency variation of 0.1 p.u. is introduced (typically, frequency variations are limited to 0.004 p.u., i.e., (50 ± 0.2) Hz). When the AC-side inductance of an ISynC-based GFM inverter is set to 50 μH, the DC voltage is capable of sensing fluctuations in the AC grid frequency. However, as the AC-side inductance increases beyond 100 μH, the DC voltage's ability to perceive these frequency fluctuations diminishes, giving rise to oscillations, as shown in Fig. 8.

Furthermore, in order to verify the effectiveness of the optimal design of inductance, the active power is changed from 0.8 p.u. to 1.0 p.u. In scenarios where active power experiences extremely fluctuations, maintaining the AC-side inductance at 50 μH ensures that the DC voltage remains within the pre-set threshold. Nevertheless, once the AC-side inductance exceeds 100 μH, the DC voltage becomes susceptible to active power fluctuations, as demonstrated in Fig. 9. Regarding variations in AC voltage amplitude, the DC voltage remains within the preset threshold when the AC-side inductance is 50 μH. However,

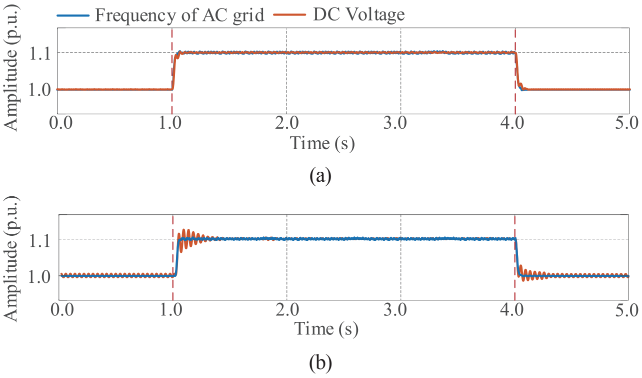

(a)

(b)

Fig. 8. DC voltage fluctuation when AC gird frequency changes. (a) $L_f = 50$ μH, (b) $L_f = 100$ μH.

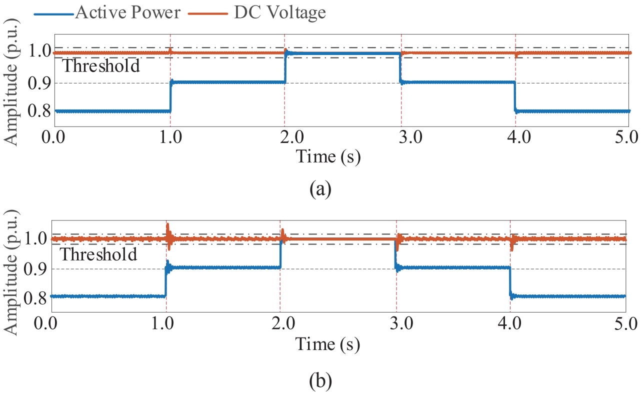

(a)

(b)

Fig. 9. DC voltage fluctuation when active power changes. (a) $L_f = 50$ μH, (b) $L_f = 100$ μH.

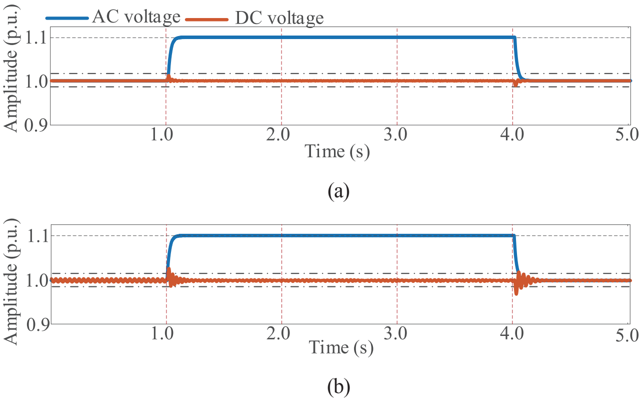

(a)

(b)

Fig. 10. DC voltage fluctuation when AC voltage changes. (a) $L_f = 50$ μH, (b) $L_f = 100$ μH.

as the AC-side inductance gradually increases, the DC voltage becomes sensitive to fluctuations in AC voltage amplitude, as shown in Fig. 10.

V. EXPERIMENTAL RESULTS

To further verify the effectiveness of the proposed optimized design method for AC-side inductance, the real-time hardware-in-the-loop (HIL) experimental platform has been constructed, as shown in Fig. 11.

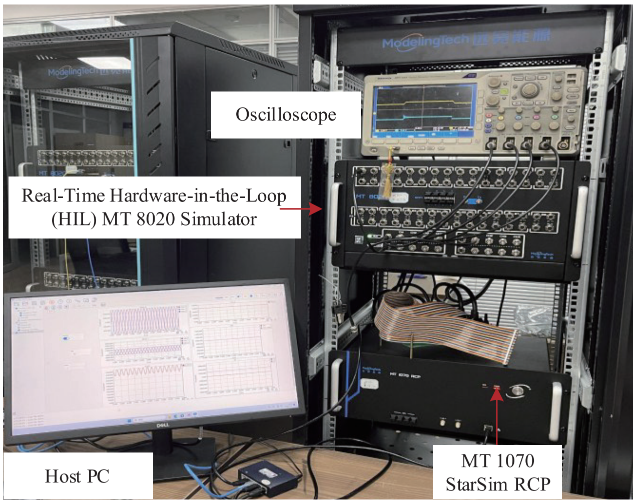

Fig. 11. HIL experimental platform.

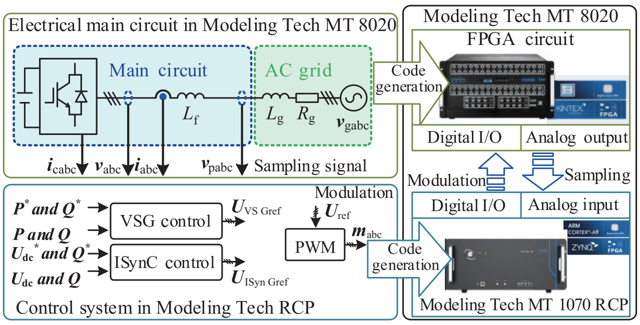

Fig. 12. Implementation scheme of HIL experiment platform for grid-connected inverter.

As illustrated in Fig. 12, the main circuit is imported by the host PC via StarSim HIL software into the FPGA of the real time simulator (Modeling Tech, MT 8020), which runs in closed-loop connection with the StarSim rapid control prototyping (RCP, Modeling Tech, Dual-core ARM Cortex-A9, MT 1070, Main Frequency 800 MHz) controller via a connection box, and the waveform output is presented by an oscilloscope. The RCP can sample the current and voltage signals from the main circuits and import the digital control signals back to the power circuits in FPGA for controlling, which ensures a closed-loop system. The main circuit parameters and control parameters of HIL experimental platform are the same with that in simulations.

A. HIL Experimental Verification for VSG-Based Inverter

The main circuit of VSG-based inverter in Fig. 1 is imported into the Modeling Tech MT 8020 FPGA, and the DC side is replaced by a DC voltage source. VSG control of Fig. 1 is imported into Modeling Tech RCP. Under the certain condition of the ac grid, power coupling can be decreased with increasing the AC-side inductance of VSG-based inverter, as shown in Fig. 13.

If the AC-side inductance is 20 μH, when the active power reference is changed from 0.7 p.u. to 1.0 p.u., power coupling

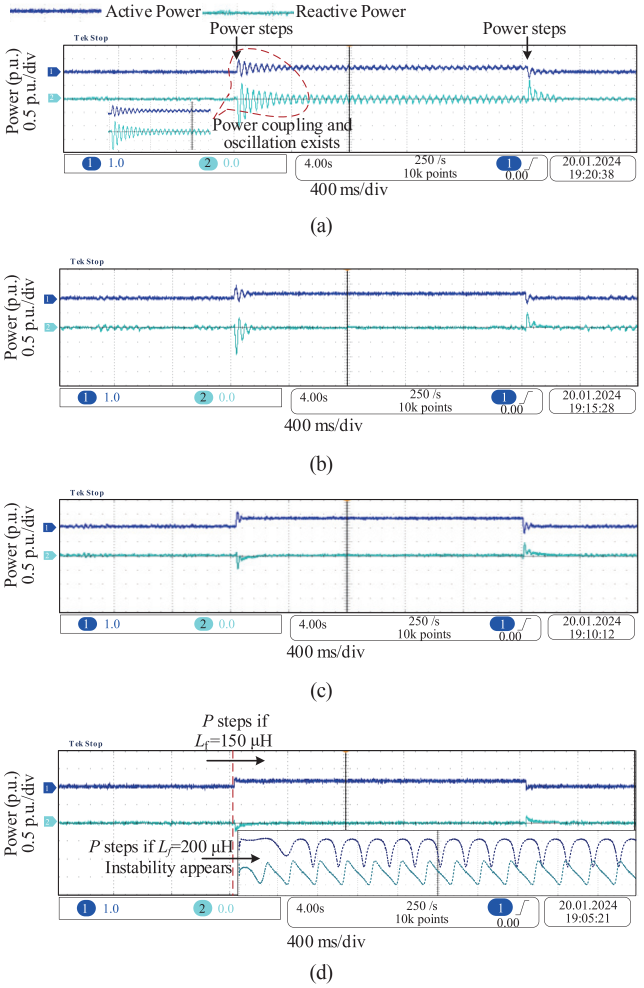

Fig. 13. Power waveforms when active power changes. (a) L_f= 20 μH, (b) L_f= 50 μH, (c) L_f= 100 μH, (d) L_f= 150 or 200 μH.

is apparent and the oscillation will appear, as shown in Fig. 13(a). When the AC-side inductance value is increased to 50 μH, the extent of power coupling and oscillation is reduced, as depicted in Fig. 13(b). When the AC-side inductance value is raised to 100 μH or 150 μH, a significant suppression of power coupling and oscillation is observed, as illustrated in Fig. 13 (c) and (d). However, if the AC-side inductance reaches 200 μH, power instability emerges when the active power reference shifts to rated power, as exhibited in Fig. 13(d). Therefore, if the lower limit of the AC-side inductance is only designed based on the harmonic suppression capability, the power coupling and oscillation will be apparent if the AC-side inductance is between 16.280 μH and 41 μH. However, by adopting the proposed optimal design approach for the AC-side inductance, the system can exhibit improved dynamic characteristics.

B. HIL Experimental Verification for ISynC-Based Inverter

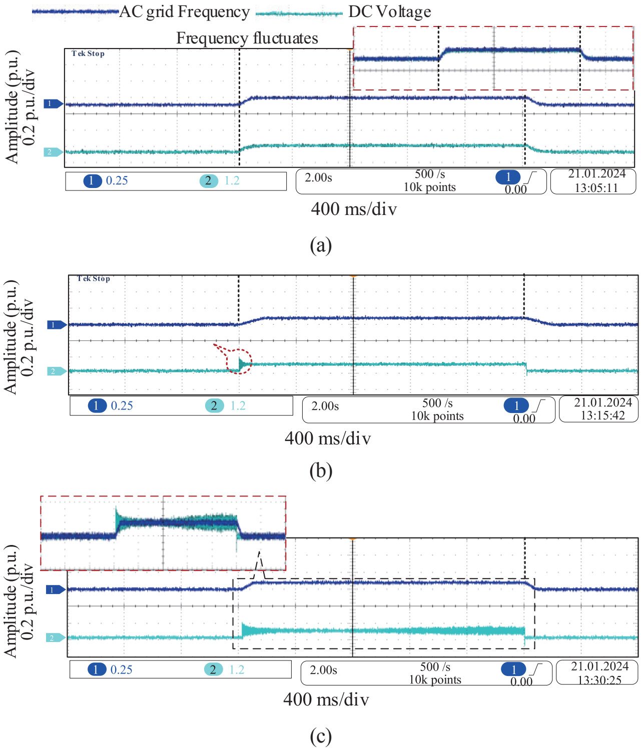

Fig. 14. DC voltage fluctuation when the AC gird frequency changes, (a) L_f= 50 μH, (b) L_f= 100 μH, (c) L_f= 150 μH.

The main circuit of ISynC-based inverter in Fig. 2 is imported into the Modeling Tech MT 8020 FPGA, and the DC side is replaced by a DC current source and a DC capacitor. ISynC control of Fig. 2 is imported into Modeling Tech RCP. The AC grid frequency is artificially changed from 1.0 p.u. to 1.1 p.u. (with a base value of 50 Hz). If the AC-side inductance is 50 μH which is within the optimal design range, the DC voltage can accurately sense the fluctuation of the grid frequency in time, as shown in Fig. 14(a). If the AC-side inductance exceeds the optimal design range, the DC voltage cannot accurately sense the frequency fluctuation. And the oscillation will gradually appear in the DC voltage, as shown in Figs. 14(b) and (c).

Setting the AC grid frequency is 1.0 p.u. and the amplitude of AC voltage is 1.0 p.u., active power is artificially changed from 0.8 p.u. to 1.0 p.u. If the AC-side inductance is 50 μH, the DC voltage is less influenced by changing active power, as shown in Fig. 15(a). If the AC-side inductance exceeds the optimal design range, DC voltage is gradually largely influenced by the active power fluctuation, as shown in Figs. 15(b) and (c). Similarly, setting the AC grid's frequency and active power are constant standing at 1.0 p.u., AC voltage is artificially changed from 1.0 p.u. to 1.1 p.u., DC voltage is gradually largely influenced by the AC voltage fluctuation with increasing the AC side inductance, as shown in Fig. 16. Therefore, if the AC-side inductance is only designed based on the harmonic suppression capability and the power transfer constraints, the DC voltage of the ISynC-based GFM inverter may fail to accurately sense fluctuations in the grid frequency. Also, DC voltage is susceptible to disturbance caused by fluctuations in AC voltage and active power. However, by adopting the proposed optimal design approach for the AC-side inductance, the DC voltage can exhibit improved dynamic characteristics.

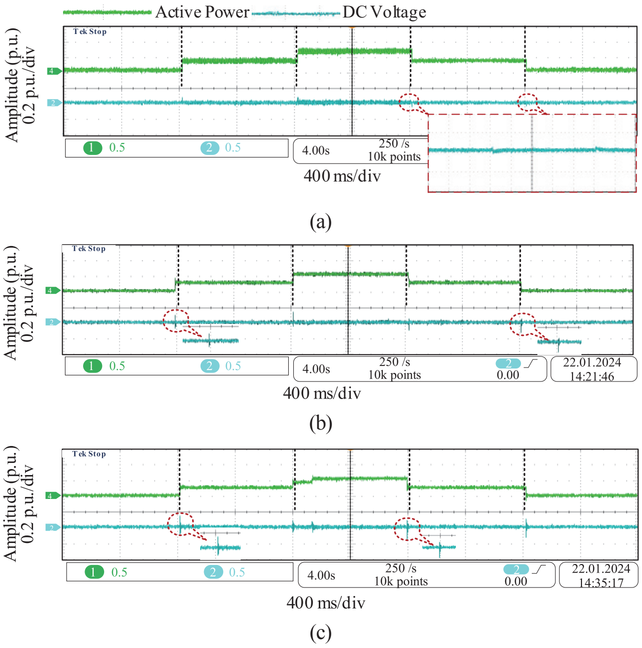

(a)

(b)

(c)

Fig. 15. DC voltage fluctuation when the active power changes. (a) L_f= 50 μH, (b) L_f= 100 μH, (c) L_f= 150 μH.

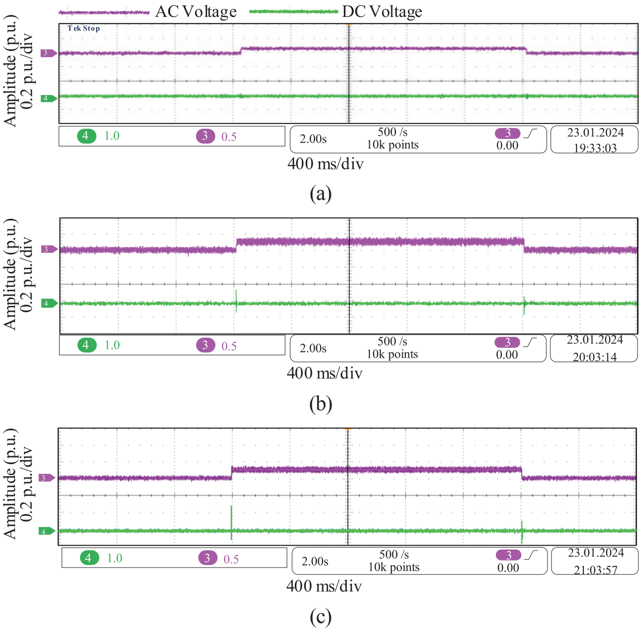

(a)

(b)

(c)

Fig. 16. DC voltage fluctuation when the amplitude of AC voltage changes. (a) L_f= 50 μH, (b) L_f= 100 μH, (c) L_f= 150 μH.

VI. CONCLUSION

This paper proposes an optimal design methodology for AC-side inductance to improve the dynamic performance of GFM inverters. Based on the traditional design objectives of harmonic attenuation and four-quadrant operation capability, an optimized design of AC-side inductance is introduced by considering various specific constraint conditions such as the power coupling degree of VSG-based inverters and the constraint relationships between the DC voltage and AC-side dynamics of ISynC-based inverters. Simulation and experimental results are demonstrated to validate the effectiveness of the proposed optimized design method. The proposed optimal design method can achieve the superior dynamic characteristics while avoiding trial-and-error procedures.

REFERENCES

[1] L. Gao, J. Lyu, X. Zong, X. Cai, and M. Molinas, “Online oscillatory stability assessment of renewable energy integrated systems based on data-driven and knowledge-driven method,” in *IEEE Transactions on Power Delivery*, vol. 40, no. 4, pp. 2072–2085, Aug. 2025.

[2] X. Wang, M. G. Taul, H. Wu, Y. Liao, F. Blaabjerg, and L. Harnefors, “Grid-synchronization stability of converter-based resources—an overview” in *IEEE Open Journal of Industry Applications*, vol. 1, pp. 115–134, 2020.

[3] L. Gao, J. Lyu, X. Zong, H. Wang, and X. Cai, “Reactive power hybrid synchronization control for oscillatory stability enhancement of grid connected inverters under ultra-weak grids,” in *IEEE Transactions on Power Electronics*, vol. 40, no. 11, pp. 16837–16852, Nov. 2025.

[4] R. H. Lasseter, Z. Chen, and D. Pattabiraman, “Grid-forming inverters: A critical asset for the power grid,” in *IEEE Journal of Emerging and Selected Topics in Power Electronics*, vol. 8, no. 2, pp. 925–935, Jun. 2020.

[5] R. Rosso, X. Wang, M. Liserre, X. Lu, and S. Engelken, “Grid-forming converters: control approaches, grid-synchronization, and future trends—a review,” in *IEEE Open Journal of Industry Applications*, vol. 2, pp. 93–109, 2021.

[6] M. Yang, Y. Wang, X. Xiao, and Y. Li, “A robust damping control for virtual synchronous generators based on energy reshaping,” in *IEEE Transactions on Energy Conversion*, vol. 38, no. 3, pp. 2146–2159, Sept. 2023.

[7] P. Sun, J. Yao, Y. Zhao, X. Fang, and J. Cao, “Stability assessment and damping optimization control of multiple grid-connected virtual synchronous generators,” in *IEEE Transactions on Energy Conversion*, vol. 36, no. 4, pp. 3555–3567, Dec. 2021.

[8] Y. Rao, J. Lyu, H. Wang, and X. Cai, “Comparative study of coupling characteristics between machine- and grid-side subsystems of PMSG based WTGS under different control modes,” in *Proceedings of 2023 IEEE 14th International Symposium on Power Electronics for Distributed Generation Systems (PEDG)*, pp. 299–306, Jun. 2023.

[9] L. Zhao, Z. Jin, and X. Wang, “Analysis and damping of low-frequency oscillation for dc-link voltage-synchronized VSCs,” in *IEEE Transactions on Power Electronics*, vol. 38, no. 7, pp. 8177–8189, Jul. 2023.

[10] L. Harnefors, M. Hinkkanen, U. Riaz, F. M. M. Rahman, and L. Zhang, “Robust analytic design of power-synchronization control,” in *IEEE Transactions on Industrial Electronics*, vol. 66, no. 8, pp. 5810–5819, Aug. 2019.

[11] Y. Yang, Y. Ruan, H. Shen, Y. Tan, and Y. Yang, “The design of inductance in AC side of grid-connected inverter in wind power generation,” in *Proceedings of 2008 International Conference on Electrical Machines and Systems,* Wuhan, pp. 2464–2469, 2008.

[12] G. Lou, Q. Yang, W. Gu, X. Quan, J. M. Guerrero, and S. Li, “Analysis and design of hybrid harmonic suppression scheme for VSG considering nonlinear loads and distorted grid,” in *IEEE Transactions on Energy Conversion*, vol. 36, no. 4, pp. 3096–3107, Dec. 2021.

[13] Y. Cai, Y. He, H. Zhou, and J. Liu, “Design method of LCL filter for grid-connected inverter based on particle swarm optimization and screening method,” in *IEEE Transactions on Power Electronics*, vol. 36, no. 9, pp. 10097–10113, Sept. 2021.

[14] Y. Jiao and F. C. Lee, “LCL filter design and inductor current ripple analysis for a three-level NPC grid interface converter,” in *IEEE Transactions on Power Electronics*, vol. 30, no. 9, pp. 4659–4668, Sept. 2015.

[15] P. Yao and X. Jiang, "Optimal six vector switching pattern in matrix converters for reducing harmonics and switching loss," in *CSEE Journal of Power and Energy Systems*, vol. 9, no. 1, pp. 135–144, Jan. 2023.

[16] B. Long, W. Yang, Q. Hu, J. M. Guerrero, C. Garcia, J. Rodriguez, and K. T. Chong, "Moth-flame-optimization-based parameter estimation for FCS-MPC-controlled grid-connected converter with LCL filter," in *IEEE Journal of Emerging and Selected Topics in Power Electronics*, vol. 10, no. 4, pp. 4102–4114, Aug. 2022.

[17] S. Bagawade, I. Askarian, M. Pahlevani, and P. Jain, "A new discrete four quadrant control technique for grid-connected full-bridge AC–DC converters," in *IEEE Journal of Emerging and Selected Topics in Power Electronics*, vol. 10, no. 2, pp. 2362–2379, Apr. 2022.

[18] Z. Guo, H. Wang, Y. Cao, and X. Cai, "Four-quadrant operation for selfsynchronous voltage source PWM converter," in *Proceedings of 2024 IEEE 10th International Power Electronics and Motion Control Conference (IPEMC2024-ECCE Asia)*, Chengdu, China, 2024, pp. 389–394.

[19] K. A. Joshi and N. M. Pindoriya, "Case-specificity and its implications in distribution network analysis with increasing penetration of photovoltaic generation," in *CSEE Journal of Power and Energy Systems*, vol. 3, no. 1, pp. 101–113, Mar. 2017.

[20] I. J. Gabe, V. F. Montagner, and H. Pinheiro, "Design and implementation of a robust current controller for VSI connected to the grid through an LCL filter," in *IEEE Transactions on Power Electronics*, vol. 24, no. 6, pp. 1444–1452, Jun. 2009.

[21] Z. Gong, C. Liu, L. Shang, Q. Lai, and Y. Terriche, "Power decoupling strategy for voltage modulated direct power control of voltage source inverters connected to weak grids," in *IEEE Transactions on Sustainable Energy*, vol. 14, no. 1, pp. 152–167, Jan. 2023.

[22] S. Sang, C. Zhang, X. Cai, M. Molinas, J. Zhang, and F. Rao, "Control of a type-IV wind turbine with the capability of robust grid-synchronization and inertial response for weak grid stable operation," in *IEEE Access*, vol. 7, pp. 58553–58569, May 2019.

[23] N. Baeckeland, D. Chatterjee, M. Lu, B. Johnson, and G. -S. Seo, "Overcurrent limiting in grid-forming inverters: A comprehensive review and discussion," in *IEEE Transactions on Power Electronics*, vol. 39, no. 11, pp. 14493–14517, Nov. 2024.

[24] M. Li, Y. Wang, W. Hu, S. Shu, P. Yu, Z. Zhang, and F. Blaabjerg, "Unified modeling and analysis of dynamic power coupling for grid-forming converters," in *IEEE Transactions on Power Electronics*, vol. 37, no. 2, pp. 2321–2337, Feb. 2022.

[25] K. Ji, H. Lu, and M. Wang, "A vector-power synchronization control for grid-forming voltage-source converters with enhanced performance under wide SCR condition," in *IEEE Transactions on Power Delivery*, vol. 39, no. 4, pp. 2507-2519, Aug. 2024.

[26] D. B. Rathnayake and B. Bahrani, "Multivariable control design for grid forming inverters with decoupled active and reactive power loops," in *IEEE Trans. on Power Electron*, vol. 38, no. 2, pp. 1635–1649, Feb. 2023.

[27] Y. Qin, H. Wang, Z. Deng, J. Zhang, R. Yang, and X. Cai, "Control of inertia-synchronization controlled wind turbine generators under symmetrical grid faults," in *IEEE Transactions on Power Electronics*, vol. 38, no. 2, pp. 1085–1096, Jun. 2023.

[28] P. Koralewicz, S. Shah, V. Gevorgian, R. Wallen, K. Jha, D. Mashtare, K. V. R. Gadiraju, and A. Tiwari, "Impedance analysis and PHIL demonstration of reactive power oscillations in a wind power plant using a 4-MW wind turbine," in *Frontiers in Energy Research*, vol. 8, no. 156, Jul. 2020.

[29] P. Kundur, N. J. Balu, and M. G. Lauby, in *Power system stability and control*. New York, NY, USA: McGraw-hill, 1994.

[30] S. Shah and L. Parsa, "Impedance modeling of three-phase voltage source converters in DQ, sequence, and phasor domains," in *IEEE Transactions on Energy Conversion*, vol. 32, no. 3, pp. 1139–1150, Sept. 2017.

[31] F. Liu, J. Liu, H. Zhang, D. Xue, H. S. UI, and L. Zhou, "Modified norm type stability criterion for cascade AC system," in *Proceedings of 2013 IEEE Energy Conversion Congress and Exposition*, Denver, CO, USA, pp. 442–447, Sept. 2013.

Lei Gao received the M.Eng. degree in electrical engineering from North China Electric Power University, Beijing, China, in 2022. He is currently working toward the Ph.D. degree in electrical engineering with Shanghai Jiao Tong University, Shanghai, China. His research interests include oscillatory stability of offshore wind farms integration via MMC-HVDC and online stability assessment and active suppression of wideband oscillations in renewable power systems.

Jing Lyu received the B.Eng. degree in electrical engineering and automation from China University of Mining and Technology, Jiangsu, China, in 2009, the M.Eng. and Ph.D. degrees from Shanghai Jiao Tong University, Shanghai, China, in 2011 and 2016, respectively, both in electrical engineering. From 2016 to 2017, he was a Postdoctoral Research Fellow with the Department of Engineering Cybernetics, Norwegian University of Science and Technology, Trondheim, Norway. Since 2018, he has been with the School of Electrical Engineering, Shanghai Jiao Tong University, where he is currently a tenured Associate Professor. His research interests include dynamic stability of power electronics-based power systems, wind power generation, HVDC transmission, and application of artificial intelligence in stability of renewable power systems.

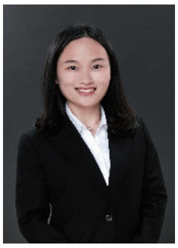

Jinshui Dai received the B.Eng. degree in electrical engineering and automation from China University of Mining and Technology, Jiangsu, China, in 2009, the M.Eng. degree in electrical engineering from Southeast University, Nanjing, China, in 2012. During 2012−2013, she was a R&D Engineer at Shanghai Electric Wind Power Group Co., Ltd.. Since 2013, she has been with the School of Electrical Engineering, Shanghai Jiao Tong University. Her main research interests include renewable power generation, modeling and control of power electronic converters.

Han Wang received the B.Sc. degree from China University of Mining and Technology, Beijing, China, in 2005, the M.Sc. and Ph.D. degrees from Shanghai Jiao Tong University, Shanghai, China, in 2008 and 2013, respectively, all in electrical engineering. During 2014–2019, he was an Engineer with Shanghai Mitsubishi Elevator Company, Shanghai Electric Group. From 2019 to now, he is a Postdoctoral Research Fellow in the School of Electrical Engineering, Shanghai Jiao Tong University, Shanghai, China. His research interests include high power converters, renewable energy generation and grid integration.

Xu Cai received the B.Eng. degree in electrical engineering from Southeast University, Nanjing, China, in 1983, the M.Eng. and Ph.D. degrees from China University of Mining and Technology, Jiangsu, China, in 1988 and 2000, respectively, both in electrical engineering. He was with the School of Electrical Engineering, China University of Mining and Technology, as an Associate Professor from 1989 to 2001. Since 2002, He has been with Shanghai Jiao Tong University, Shanghai, as a Professor, where he has also been the Director of the Wind Power Research Center since 2008. His current research interests include large power electronics, wind power generation and grid integration, HVDC, large power battery storage systems, etc.